Spontaneous Interface Layer Engineering of $Ag_2Mn_8O_{16}$ Cathode via Anodic Oxidation Strategy toward High-Performance Aqueous Zinc-Ion Batteries

Xiaodong Shi,[#] Chuancong Zhou,[#] Fuhua Yang, Lutong Shan,[*] Boya Tang, Jie Zhang, Qing Nan, Yu Xie, Jing Li, Huangxu Li,[*] and Xinlong Tian[*]

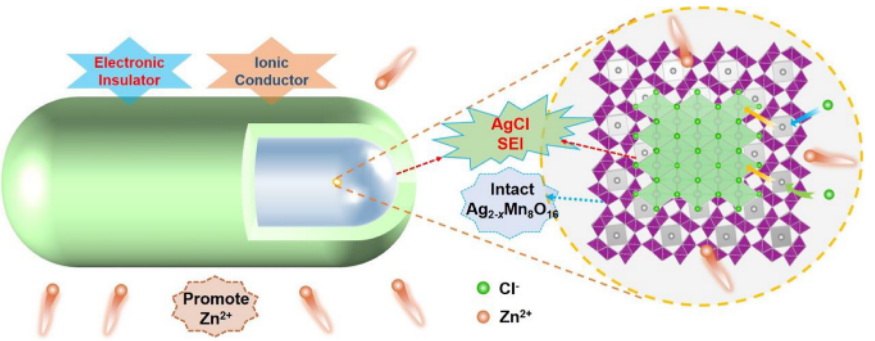

ABSTRACT: **The disproportionation reaction of Mn^{3+} ions induced by the Jahn−Teller effect hinders the practical application of Mn-based oxides in aqueous zinc-ion batteries (AZIBs). Herein, $Ag_2Mn_8O_{16}$ is reported as a promising cathode for AZIBs, and its performance improvement mechanism in a chlorine-containing electrolyte is comprehensively investigated. As demonstrated, the partial deintercalation of silver ions promotes the valence state and reactivity of the Mn element in $Ag_{2-x}Mn_8O_{16}$ and favors the formation of the AgCl layer. As an electronic insulator and ionic conductor, the AgCl layer can effectively inhibit the manganese dissolution, reduce the activation energy barrier, and facilitate the zinc diffusion kinetics in $Ag_2Mn_8O_{16}$. As expected, the $Ag_2Mn_8O_{16}$ cathode exhibits high capacity of 369.2 mAh g^{-1} at 0.1 A g^{-1} and 269.6 mAh g^{-1} after 200 cycles at 0.5 A g^{-1} in the optimized chlorine-containing electrolyte, implying the *in situ* interface engineering can eliminate the dilemma of dissolution and inactivation of Mn-based oxides in aqueous batteries.**

Aqueous zinc-ion batteries (AZIBs) have attracted wide attention because of their characteristics of low cost, high safety, and high capacity.[1−4] Mn-based oxide materials hold various oxidation states and crystal structure, such as tunnel structure, layered structure, and three-dimensional spatial framework, which can provide enough space to accommodate zinc ions.[5,6] In addition, Mn-based oxides have the unique advantages of abundant resources, low toxicity, high operating potential, and high theoretical capacity[7] and have been considered as the most promising cathode materials for zinc storage.[8−10]

However, the practical applications of Mn-based oxide cathode materials in AZIBs are still restricted by the inherent low conductivity, slow diffusion kinetics, and poor structural stability.[11] In particular, the disproportionation reaction of Mn^{3+} ions aroused by the Jahn−Teller effect[12−14] always induces manganese dissolution and structural collapse of Mn-based compounds in an aqueous electrolyte, thereby leading to the voltage drop, capacity attenuation, and asymmetric changes in the Mn−O bond length of octahedral $Mn^{3+}O_6$ and

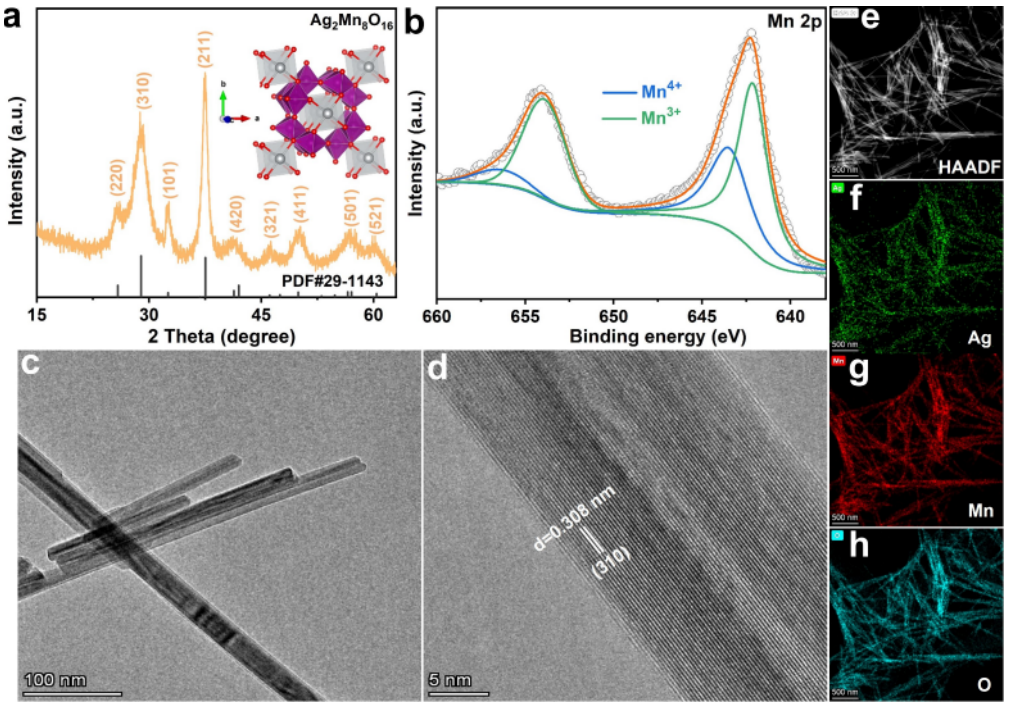

Figure 1. (a) XRD patterns, (b) Mn 2p XPS spectra, (c) TEM image, (d) HRTEM image, (e) HAADF image, and (f–h) the elemental mapping images of $Ag_2Mn_8O_{16}$ raw material.

$Mn^{4+}O_6$.[15,16] Therefore, Mn-based oxide cathodes suffer from great challenges of active material dissolution and structural instability.[17] Interface layer engineering is an effective strategy to improve the interfacial stability,[18−20] which can not only reduce the direct contact between Mn-based oxide cathodes and aqueous electrolytes to ease the manganese dissolution but also enhance the electron charge and ion transfer on the surface of the cathode material.[21−23] Currently, carbonaceous materials,[24−26] organic polymer materials,[27−30] and inorganic nonmetallic materials[31,32] have been adopted as the coating layers to modify the surface of Mn-based oxide cathodes, which play different roles to improve the battery performance to a certain extent. Unfortunately, the inhibition of manganese dissolution and the Jahn−Teller effect by these artificial interface layers is at the cost of sacrificing the mass loading of active materials and blocking the transport channel of zinc ions, which reduce the zinc storage capacity of Mn-based oxide cathodes and weaken the diffusion kinetics of zinc ions.

Considering the positive role of the solid electrolyte interface (SEI) film in nonaqueous Li/Na-ion batteries,[33−35] *in situ* construction of the SEI layer on the surface of Mn-based oxide cathodes can effectively guarantee fast diffusion kinetics of zinc ions, suppress the dissolution of active component, and give full play to the battery performance. As a typical case, a $CaSO_4{\cdot}2H_2O$ thin layer is spontaneously constructed on the surface of Ca_2MnO_4 cathode through the initial charge process to 1.8 V in the $ZnSO_4$-based electrolyte for AZIBs.[36] As expected, the robust $CaSO_4{\cdot}2H_2O$ layer possesses the intrinsic properties of electronic insulation and ionic conductor, thereby inhibiting the manganese dissolution, reducing the activation energy barrier, and facilitating the reversible (de)intercalation of zinc ions.

Inspired by this key point, $Ag_2Mn_8O_{16}$ material is prepared by the common hydrothermal method and comprehensively demonstrated as a promising cathode in the chlorine-containing electrolyte for AZIBs owing to the spontaneous formation of interface layer during the initial charge process. In particular, the partial extraction of silver ions from $Ag_2Mn_8O_{16}$ material can effectively facilitate the valence state and reactivity of Mn element, while the following precipitation reaction between silver ions and chlorine ions in the electrolyte can efficiently drive the spontaneous formation of AgCl layer, which prohibits the manganese dissolution, reduces the interface impedance, and reinforces the transport behavior of zinc ions. As a result, $Zn//Ag_2Mn_8O_{16}$ batteries can deliver a high reversible capacity of 369.2 mAh g^{-1} at 0.1 A g^{-1} and 269.6 mAh g^{-1} after 200 cycles at 0.5 A g^{-1} in a 2 M $ZnSO_4$ + 0.1 M $MnSO_4$ + 0.1 M $ZnCl_2$ electrolyte, manifesting the high zinc storage capacity and superior structural stability. This work can provide new reference for the *in situ* construction of SEI layer on the surface of cathode materials in an aqueous electrolyte and contributes to addressing the issues of dissolution loss and inactivation failure of metallic elements (Mn/V/Fe/Co/Ni etc.) with variable valence in aqueous energy storage devices.

As shown in Figure 1a, the phase composition and crystalline structure of the prepared material is characterized by X-ray diffraction (XRD) and identified as $Ag_2Mn_8O_{16}$ (PDF# 29-1143),[37] in which Ag atoms are bridged with $[MnO_6]$ polyhedrons through Ag−O bonds and firmly confined in the tunnel structure constructed by $[MnO_6]$ polyhedrons (insert image). To reveal the bonding structure and valence states of elements in $Ag_2Mn_8O_{16}$, X-ray photoelectron spectroscopy (XPS) has been employed. As presented in Figure 1b and Figure S1, Mn 2p, Ag 3d, and O 1s can be detected in the survey spectra of $Ag_2Mn_8O_{16}$ sample, while Mn 2p spectra is composed by Mn $2p_{1/2}$ (654.1 eV) and Mn $2p_{3/2}$ (642.6 eV), which can be further divided into Mn^{4+} and Mn^{3+} areas, demonstrating the mixed valence state and intrinsic high reactivity of the Mn element in $Ag_2Mn_8O_{16}$.[38] Figure S2 and

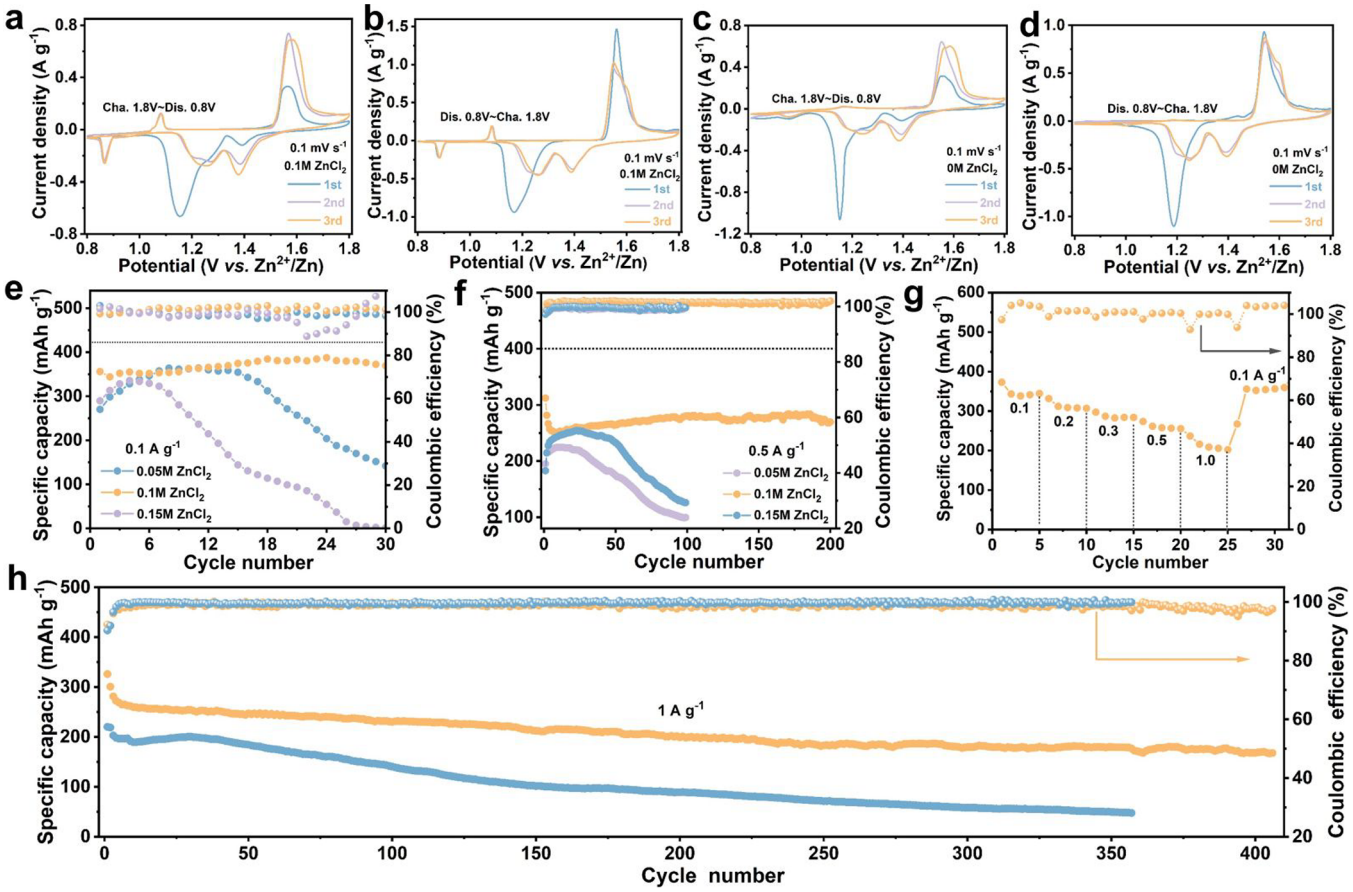

Figure 2. Normalized CV curves of $Ag_2Mn_8O_{16}$ cathode at 0.1 mV s^{-1} tested in 2 M $ZnSO_4$ + 0.1 M $MnSO_4$ + 0.1 M $ZnCl_2$ electrolyte under (a) the charge before discharge mode and (b) the discharge before charge mode, and tested in 2 M $ZnSO_4$ + 0.1 M $MnSO_4$ electrolyte under (c) the charge before discharge mode and (d) the discharge before charge mode; cycling performances of $Ag_2Mn_8O_{16}$ cathode at (e) 100 and (f) 500 mA g^{-1} in the electrolytes with different amount of $ZnCl_2$ additive (0.05 M $ZnCl_2$/0.1 M $ZnCl_2$/0.15 M $ZnCl_2$); (g) rate performance of $Ag_2Mn_8O_{16}$ cathode in 2 M $ZnSO_4$ + 0.1 M $MnSO_4$ + 0.1 M $ZnCl_2$ electrolyte at 100, 200, 300, 500, and 1000 mA g^{-1}; long-term cyclic stability of $Ag_2Mn_8O_{16}$ cathode at 1000 mA g^{-1} in chlorine-free (blue line) and chlorine-containing (orange line) electrolytes.

Figure 1c respectively represent the SEM and TEM images of $Ag_2Mn_8O_{16}$ samples and display the typical nanorod morphology of Mn-based oxides. The HRTEM image in Figure 1d presents a clear lattice spacing of 0.308 nm, corresponding to the (310) plane of $Ag_2Mn_8O_{16}$. Moreover, the mapping images in Figure 1e–h further verify the uniform distribution of Ag, Mn, and O elements in the interwoven nanorod-like $Ag_2Mn_8O_{16}$.

As a promising cathode material for AZIBs, different charge/discharge modes and electrolyte compositions have been investigated to achieve the best zinc storage performance of the $Ag_2Mn_8O_{16}$ cathode. Figure 2a,b exhibits the normalized CV curves of Zn//$Ag_2Mn_8O_{16}$ batteries in 2 M $ZnSO_4$ + 0.1 M $MnSO_4$ + 0.1 M $ZnCl_2$ (chlorine-containing) electrolyte under different charge/discharge modes. For the charge before discharge mode (Figure 2a), the oxidation peak at 1.565 V in the first anodic lap can be attributed to the local deintercalation of silver ions from the crystal framework of $Ag_2Mn_8O_{16}$,[36,39] accompanying the formation of cation defects and the increase of valence state as well as reactivity of Mn element in the residual $Ag_{2-x}Mn_8O_{16}$ cathode. Additionally, the extracted silver ions will precipitate with the chlorine ions in the electrolyte and spontaneously cover the surface of the cathode material. The moderate and sharp reduction peaks at 1.39 and 1.155 V appearing in the first cathodic lap can be ascribed to the activated insertion reaction of $Ag_{2-x}Mn_8O_{16}$ cathode by zinc ions, while the small peak at 0.862 V may be caused by the reduction reaction of chlorine ions. In the second and third lap, the couple peaks at 1.082 and 0.862 V can be attributed to the redox reaction of chlorine ions.[40,41] The prominent oxidation peak around 1.581 V and the gradient reduction peaks at 1.377 and 1.251 V respectively correspond to the deintercalation and intercalation reaction of the $Ag_{2-x}Mn_8O_{16}$ cathode.[42,43] For the discharge before the charge mode (Figure 2b), the paired peaks at 1.083/0.864 V also appear, indicating the redox reaction of chlorine ions is not affected by the charge/discharge modes.

Figure 2c,d displays the normalized CV curves of Zn//$Ag_2Mn_8O_{16}$ batteries in 2 M $ZnSO_4$ + 0.1 M $MnSO_4$ (chlorine-free) electrolyte under different charge/discharge modes. Without the addition of $ZnCl_2$, the anodic peak at 1.554 V in Figure 2c during the initial charge process is also related to the extraction of silver ions from $Ag_2Mn_8O_{16}$. Notably, the paired peaks belonging to the redox reaction of chlorine ions are absent, and the remaining redox peaks match with the reversible (de)intercalation behavior of zinc ions, suggesting the different reaction mechanism of $Ag_2Mn_8O_{16}$ in chlorine-free and chlorine-containing electrolyte. Additionally, the crystalline structure of $Ag_2Mn_8O_{16}$ and β-MnO_2 has been compared, while the normalized CV curves of the β-MnO_2

cathode at 0.1 mV s^{-1} in 2 M $ZnSO_4$ + 0.1 M $MnSO_4$ + 0.1 M $ZnCl_2$ electrolyte under the discharge before charge mode have been tested. As presented in Figure S3a,b, β-MnO_2 has the tunnel structure similar to $Ag_2Mn_8O_{16}$ only without the existence of [AgO_4] bonding planes. As for the CV curves (Figure S3c), the coupled peaks at 1.083/0.864 V ascribed to the redox reaction of chlorine ions do not appear, suggesting that the redox reaction of chlorine ions does not spontaneously occur without the participation of silver ions as well as the formation of a AgCl interface layer. Therefore, the chlorine-containing electrolyte of 2 M $ZnSO_4$ + 0.1 M $MnSO_4$ + 0.1 M $ZnCl_2$ is the optimal choice for the performance improvement of $Ag_2Mn_8O_{16}$, and the positive adsorption effect on chlorine ions at the interface between AgCl and $Ag_{2-x}Mn_8O_{16}$ can promote the redox reaction of chlorine ions and increase the additional capacity.

The effects of different amounts of $ZnCl_2$ additive on the cycling performance of Zn//$Ag_2Mn_8O_{16}$ batteries have been comprehensively disclosed (Figure 2e). In detail, the reversible capacity of $Ag_2Mn_8O_{16}$ cathode in 2 M $ZnSO_4$ + 0.1 M $MnSO_4$ + 0.1 M $ZnCl_2$ electrolyte can achieve 369.2 mAh g^{-1} after 30 cycles at 100 mA g^{-1}. In sharp contrast, the specific capacity of $Ag_2Mn_8O_{16}$ cathode in 0.05 M $ZnCl_2$ and 0.15 M $ZnCl_2$-containing electrolytes at 100 mA g^{-1} after 30 cycles only retain 141.7 mAh g^{-1} and 1.4 mAh g^{-1}, respectively, implying a severe capacity decay. In addition, the cyclic stability of the $Ag_2Mn_8O_{16}$ cathode in 2 M $ZnSO_4$ + 0.1 M $MnSO_4$ + 0.1 M $ZnCl_2$ electrolyte can be increasingly enhanced at 500 mA g^{-1}, and it can stabilize at 269.6 mAh g^{-1} after 200 cycles (Figure 2f), much higher than that in 0.05 M $ZnCl_2$ and 0.15 M $ZnCl_2$-containing electrolytes. Moreover, $Ag_2Mn_8O_{16}$ cathode also delivers inferior cycling stability and lower capacity in 2 M $ZnSO_4$ + 0.1 M $MnSO_4$ electrolyte (Figure S4), and the specific capacity only remain 73.86 mAh g^{-1} and 77.6 mAh g^{-1} after 40 and 200 cycles at 100 and 500 mA g^{-1}, respectively. These results demonstrate that moderate addition of $ZnCl_2$ in the electrolyte can effectively facilitate the zinc storage capacity and cycle life of Zn//$Ag_2Mn_8O_{16}$ batteries, and 2 M $ZnSO_4$ + 0.1 M $MnSO_4$ + 0.1 M $ZnCl_2$ electrolyte is chosen for the reaction mechanism analysis of the $Ag_2Mn_8O_{16}$ cathode. Furthermore, the Mn content of the $Ag_2Mn_8O_{16}$ cathode in chlorine-containing and chlorine-free electrolytes after 10 and 100 cycles has been measured by inductively coupled plasma-optical emission spectroscopy (ICP-OES). As presented in Table S1, the Mn content of the $Ag_2Mn_8O_{16}$ cathode in 2 M $ZnSO_4$ + 0.1 M $MnSO_4$ electrolyte decreases from 14.49 to 9.81 mg mL^{-1} between 10 and 100 cycles, verifying the presence of manganese dissolution behavior, which seriously affects the cyclic stability of the Mn-based cathode. As demonstrated in Figure S4b, the $Ag_2Mn_8O_{16}$ cathode exhibits an obvious capacity fading within 50−100 cycles in 2 M $ZnSO_4$ + 0.1 M $MnSO_4$ electrolyte at 500 mA g^{-1}. In contrast, the Mn content of $Ag_2Mn_8O_{16}$ cathode in 2 M $ZnSO_4$ + 0.1 M $MnSO_4$ + 0.1 M $ZnCl_2$ electrolyte remains nearly constant between 10 and 100 cycles, manifesting the effective inhibition of manganese dissolution of the *in situ* AgCl layer. Meanwhile, the corresponding cycling behavior of $Ag_2Mn_8O_{16}$ cathode in 2 M $ZnSO_4$ + 0.1 M $MnSO_4$ + 0.1 M $ZnCl_2$ electrolyte also keeps stable, certifying that inhibiting manganese dissolution is of great significance for boosting the structural stability and cyclic stability of Mn-based cathodes.

The positive contribution of chlorine ions also can be further demonstrated by the cycling performance of the $Ag_2Mn_8O_{16}$ cathode at 500 mA g^{-1} in 2 M $ZnSO_4$ + 0.1 M $MnCl_2$ (Figures S5), 2 M $ZnSO_4$ + 0.1 M $MnSO_4$ + 0.2 M LiCl, and 2 M $ZnSO_4$ + 0.1 M $MnSO_4$ + 0.2 M NH_4Cl (Figures S6) electrolytes. Figure 2g exhibits the rate capability of $Ag_2Mn_8O_{16}$ cathode in 2 M $ZnSO_4$ + 0.1 M $MnSO_4$ + 0.1 M $ZnCl_2$ electrolyte, and the reversible capacity is 344.7, 308.9, 284.1, 257.6, and 208.8 mAh g^{-1} at 100, 200, 300, 500, and 1000 mA g^{-1}. After recovering to 100 mA g^{-1}, the specific capacity can come back to 354.4 mAh g^{-1}. In contrast, the zinc storage capacity in the 2 M $ZnSO_4$ + 0.1 M $MnSO_4$ electrolyte (Figure S7) is only 61.7 mAh g^{-1} at 1000 mA g^{-1}. Meanwhile, the rate performances of the $Ag_2Mn_8O_{16}$ cathode in 2 M $ZnSO_4$ + 0.1 M $MnSO_4$ + 0.2 M LiCl and 2 M $ZnSO_4$ + 0.1 M $MnSO_4$ + 0.2 M NH_4Cl electrolyte (Figure S8) are also better than that in the chlorine-free electrolyte, implying the enhanced rate capability by chlorine ions. In addition, the long-term cycling performance of the $Ag_2Mn_8O_{16}$ cathode in chlorine-containing and chlorine-free electrolyte (Figure 2h) also shows a significant difference, in which the corresponding capacity stabilize at 167.8 mAh g^{-1} after 409 cycles and 47.7 mAh g^{-1} after 357 cycles at 1000 mA g^{-1}, respectively, verifying the superior cycling stability in the chlorine-containing electrolyte. The zinc storage performances of the $Ag_2Mn_8O_{16}$ cathode, including specific capacity and cycling stability, also have been compared with the previous Mn-based oxide cathodes (Table S2), and the higher capacity as well as stability of the $Ag_2Mn_8O_{16}$ cathode in chlorine-containing electrolyte further demonstrate the effectiveness of *in situ* AgCl interface strategy. Furthermore, the manganese dissolution inhibition effect of the AgCl layer is also demonstrated without the addition of $MnSO_4$ in the electrolyte. Figures S9a,b compare the normalized CV curves of Zn//$Ag_2Mn_8O_{16}$ batteries in 2 M $ZnSO_4$ + 0.1 M $ZnCl_2$ and 2 M $ZnSO_4$ electrolyte, which are similar to the CV curves in 2 M $ZnSO_4$ + 0.1 M $MnSO_4$ + 0.1 M $ZnCl_2$ electrolyte (Figure 2a) and 2 M $ZnSO_4$ + 0.1 M $MnSO_4$ electrolyte (Figure 2c). Figure S9c exhibits the cycling performance of Zn//$Ag_2Mn_8O_{16}$ batteries at 500 mA g^{-1} in 2 M $ZnSO_4$ + 0.1 M $ZnCl_2$ and 2 M $ZnSO_4$ electrolyte. Notably, Zn//$Ag_2Mn_8O_{16}$ batteries exhibit a sharp capacity decay from 254.2 to 50.81 mAh g^{-1} within 50 cycles in the 2 M $ZnSO_4$ electrolyte, verifying the positive effect of the introduction of Mn^{2+} ions on the cyclic stability of Mn-based cathodes for AZIBs.[1−3] In contrast, Zn//$Ag_2Mn_8O_{16}$ batteries display a relatively stable cycling behavior, and the corresponding capacity drops from 257.6 to 200.7 mAh g^{-1} within 100 cycles in the 2 M $ZnSO_4$ + 0.1 M $ZnCl_2$ electrolyte, demonstrating the manganese dissolution inhibition effect of the AgCl layer. In addition, the cycling performance of Zn//$Ag_2Mn_8O_{16}$ batteries in the 2 M $ZnSO_4$ + 0.1 M $MnSO_4$ + 0.1 M $ZnCl_2$ electrolyte (Figure 2f) is more stable than that in the 2 M $ZnSO_4$ + 0.1 M $ZnCl_2$ electrolyte, manifesting that the synergistic effect of Mn^{2+} ions in the electrolyte and the AgCl layer on the $Ag_2Mn_8O_{16}$ cathode can effectively promote the structural stability and cycling stability of Mn-based cathodes for AZIBs.

Moreover, the influences of charge/discharge modes on the zinc storage performance of the $Ag_2Mn_8O_{16}$ cathode in chlorine-containing electrolyte are further revealed. As exhibited in Figure S10, the corresponding specific capacity of the $Ag_2Mn_8O_{16}$ cathode adopting the discharge before charge mode is lower than that of charge before discharge mode (Figure 2) under the same test conditions, implying that the partial deintercalation of silver ions from the $Ag_2Mn_8O_{16}$

material can effectively facilitate the valence state and reactivity of the Mn element and accommodate more zinc ion storage. Thus, charge before discharge mode is also a key factor determining the zinc storage capacity of $Ag_2Mn_8O_{16}$ cathode and is employed for the further analysis of reaction kinetics and reaction mechanism. As a brief summary, the superior cycling durability and rate capability in the chlorine-containing electrolyte can be attributed to the spontaneous formation of a AgCl layer with the characteristics of electronic insulation and ionic conductor, which plays the role of an SEI film and suppresses the manganese dissolution and structural changes of the $Ag_2Mn_8O_{16}$ cathode during the cycling process.[44]

To identify the changes in electrochemical impedances and diffusion coefficients of Zn^{2+} ions (D_{Zn}) during the formation of the AgCl layer, the corresponding Nyquist plots and fitting lines of $-Z''$ with $\omega^{-1/2}$ profiles of the $Ag_2Mn_8O_{16}$ cathode in the 2 M $ZnSO_4$ + 0.1 M $MnSO_4$ + 0.1 M $ZnCl_2$ electrolyte at different charge and discharge potentials are depicted in Figure 3a,b. In brief, the charge transfer resistances (R_{ct}) at the

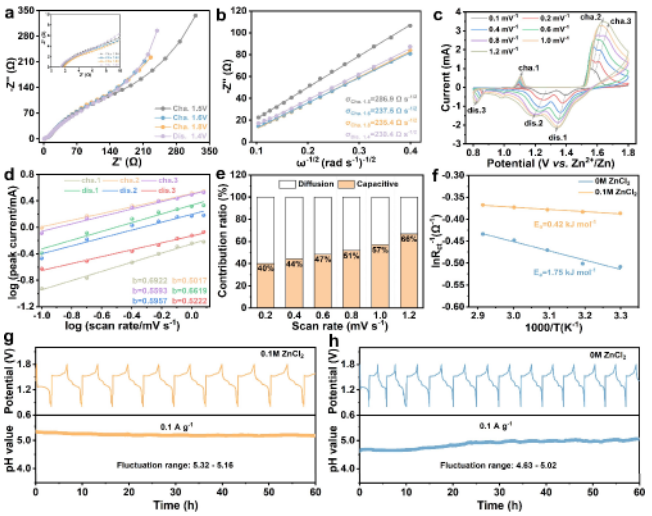

Figure 3. (a) Nyquist plots and (b) the corresponding Warburg factors of $Ag_2Mn_8O_{16}$ cathode at different charged and discharged states; (c) CV curves of $Ag_2Mn_8O_{16}$ cathode at different scan rates (0.1−1.2 mV s^{-1}) and (d) the corresponding *b* values for the redox peaks; (e) capacitive contribution ratio of $Ag_2Mn_8O_{16}$ cathode at different scan rates (0.1−1.2 mV s^{-1}); (f) activation energy of $Ag_2Mn_8O_{16}$ cathode at fully charged state in chlorine-containing (orange line) and chlorine-free (blue line) electrolytes determined by Arrhenius equation; *in situ* pH changes of Zn//$Ag_2Mn_8O_{16}$ batteries in (g) chlorine-containing and (h) chlorine-free electrolytes tested in electrolytic tank at 100 mA g^{-1}.

middle-high frequency region (inset image of Figure 3a) have little differences, indicating the newly generated AgCl layer in the initial charge process does not disturb the subsequent charge transfer behavior. Based on eqs S1−S3 and Figure 3b, the Warburg parameter (σ) can be determined by the fitting slope of $-Z''$ with $\omega^{-1/2}$, which is directly related to the straight line in the low-frequency region of Nyquist plots and inversely proportional to the D_{Zn} value (eq S3). The σ values at the charged state of 1.5, 1.6, and 1.8 V, as well as the discharged state of 1.4 V are 286.9, 237.5, 235.4, and 230.4 Ω $s^{-1/2}$, respectively; that is, the diffusion coefficients of Zn^{2+} ions gradually increase with the formation of the AgCl interfacial layer, suggesting the spontaneous AgCl SEI film is conducive to the diffusion kinetics behavior of Zn^{2+} ions in the $Ag_2Mn_8O_{16}$ cathode.

In addition, as derived from Figure 3c, the reaction mechanism of $Ag_2Mn_8O_{16}$ cathode in 2 M $ZnSO_4$ + 0.1 M $MnSO_4$ + 0.1 M $ZnCl_2$ electrolyte is revealed by the CV curves measured at different scan rates (0.1−1.2 mV s^{-1}). According to eqs S4 and S5 and Figure 3d, the *b* values for the (de)intercalation reaction of Zn^{2+} ions are calculated to be 0.662/0.596 and 0.502/0.559, corresponding to the cathodic peaks (dis.1/dis.2) and anodic peaks (cha.2/cha.3), respectively. Additionally, the *b* values for the redox reactions of chlorine ions are determined to be 0.522 and 0.692, belonging to the reduction peak (dis.3) and oxidation peak (cha.1). Moreover, all of the *b* values for the redox peaks are close to 0.5, verifying that the major zinc storage capacity of the $Ag_2Mn_8O_{16}$ cathode depends on the diffusion-controlled reaction mechanism. Based on eqs S6 and S7, the capacitive and diffusion contribution ratio of $Ag_2Mn_8O_{16}$ cathode in 2 M $ZnSO_4$ + 0.1 M $MnSO_4$ + 0.1 M $ZnCl_2$ electrolyte can be quantitatively calculated and are summarized in Figure 3e. The capacitive ratio increases from 40% to 66% accompanied by the scan rates from 0.1 to 1.2 mV s^{-1}, further confirming the diffusion-controlled reaction mechanism of the $Ag_2Mn_8O_{16}$ cathode at low scan rates.[7,45] Furthermore, the Nyquist plots of the $Ag_2Mn_8O_{16}$ cathode at a fully charged state in chlorine-free and chlorine-containing electrolytes at different temperatures (30−70 °C) have been measured. In the equivalent circuit of Figure S11a, R_1 represents the solution impedance and R_2 represents the $Ag_{2-x}Mn_8O_{16}$/solution interface impedance. In the equivalent circuit of Figure S11b, R_1 represents the solution impedance and R_2 and R_3 represent the AgCl/solution and $Ag_{2-x}Mn_8O_{16}$/AgCl interface impedance, respectively. Notably, it can be detected that the $Ag_{2-x}Mn_8O_{16}$/AgCl/solution impedances in chlorine-containing electrolyte are slightly lower than that of $Ag_{2-x}Mn_8O_{16}$/solution in chlorine-free electrolyte (Table S3). Based on the Arrhenius equation (eqs S8 and S9), the calculated activation energy values (Figure 3f) of the $Ag_2Mn_8O_{16}$ cathode in chlorine-containing and chlorine-free electrolytes are 0.42 and 1.75 kJ mol^{-1}, respectively. These results demonstrate that the partial deintercalation of silver ions and the formation of a AgCl SEI layer are conducive to accelerating the charge transfer, reducing the activation energy, and promoting the interfacial reaction of $Ag_2Mn_8O_{16}$ cathode in chlorine-containing electrolyte.[11,36,46] Additionally, the pH changes of Zn//$Ag_2Mn_8O_{16}$ batteries in chlorine-containing and chlorine-free electrolytes have been monitored real time (Figure S12). As presented in Figure 3g,h, the pH values in a chlorine-containing electrolyte are more stable than that in a chlorine-free electrolyte, which can fluctuate within the narrow range of 5.16−5.32, further indicating that the resulting AgCl interface layer can relieve the pH changes of the electrolyte induced by manganese dissolution and endow the $Ag_2Mn_8O_{16}$ cathode with a stable electrochemical reaction environment.

To reveal the zinc storage mechanism of the $Ag_2Mn_8O_{16}$ cathode in 2 M $ZnSO_4$ + 0.1 M $MnSO_4$ + 0.1 M $ZnCl_2$ electrolyte, XPS, XRD, and TEM techniques have been adopted. Compared with the raw state (Figure 1b), the Mn^{4+} areas increase and the Mn^{3+} areas of Mn 2p spectra decrease at the initially charged state (Figure 4a), indicating the enhanced reactivity of the Mn element in the $Ag_{2-x}Mn_8O_{16}$ cathode.[47] This case can be caused by the deintercalation of silver ions and the generation of cation defects, thereby inducing the possibility of accommodating more zinc ions. At

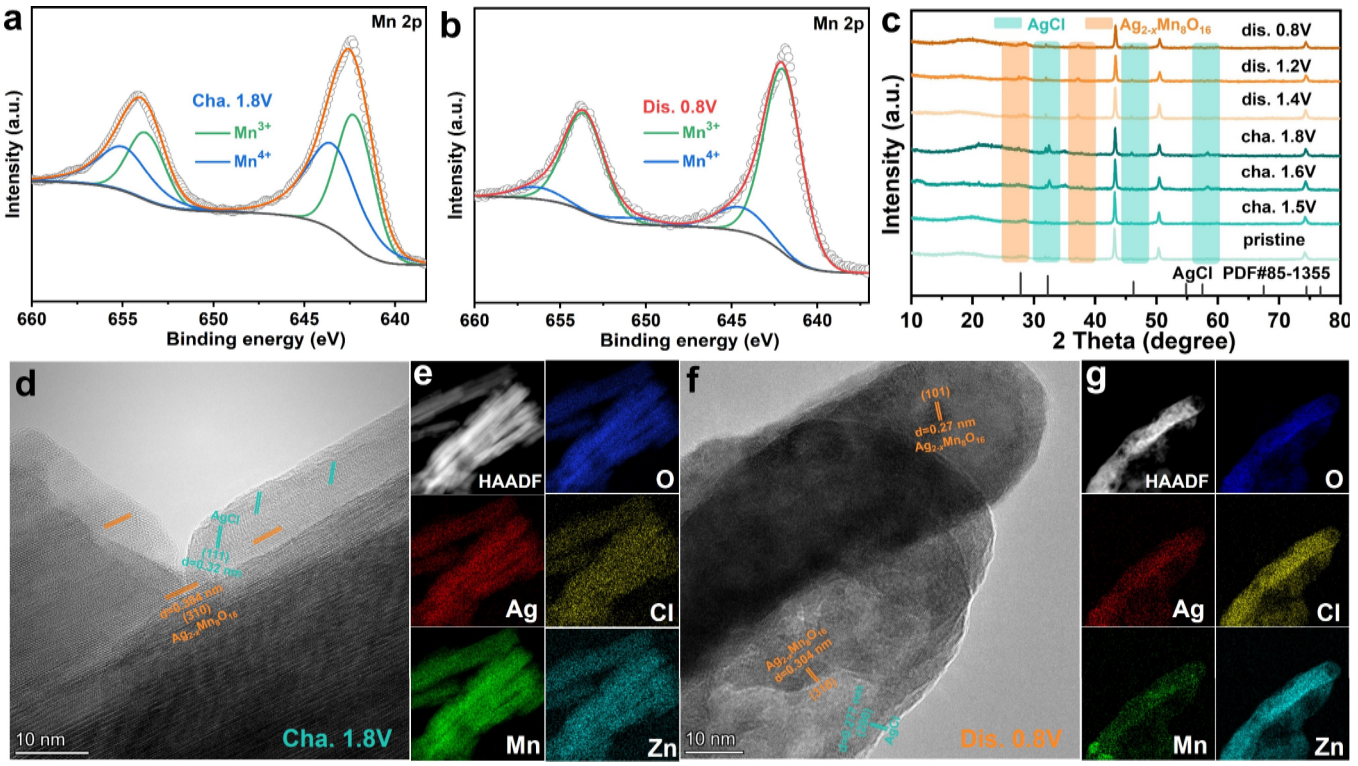

Figure 4. Mn 2p XPS spectra of $Ag_2Mn_8O_{16}$ cathode at fully (a) charged and (b) discharged states; (c) XRD patterns of $Ag_2Mn_8O_{16}$ cathode at different charged and discharged states; HRTEM images of $Ag_2Mn_8O_{16}$ cathode at fully (d) charged and (f) discharged states, as well as the corresponding elemental mapping images at fully (e) charged and (g) discharged states.

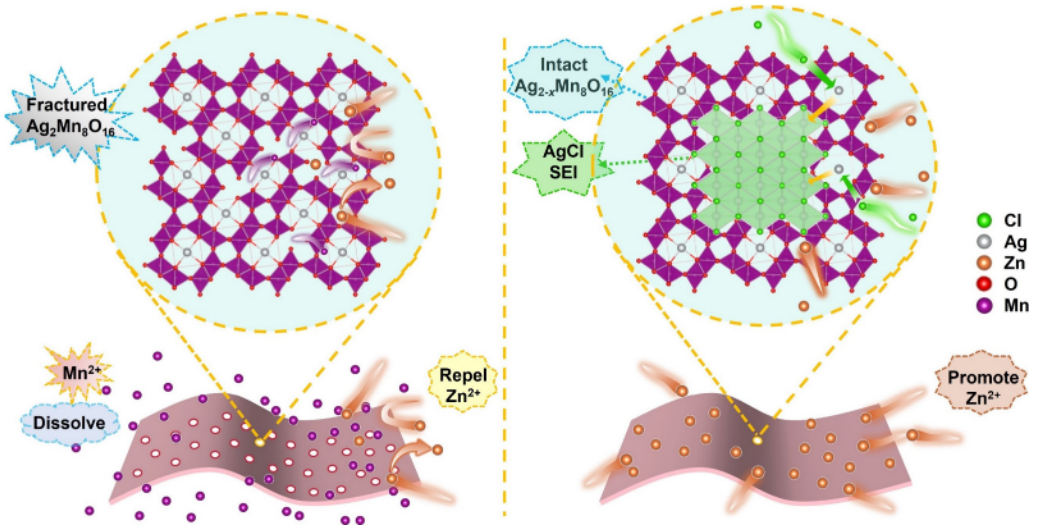

Figure 5. Schematic diagram of the protection mechanism of AgCl interface layer on the $Ag_2Mn_8O_{16}$ cathode during cycling process.

the initially discharged state (Figure 4b), most of the Mn^{4+} areas in Mn 2p spectra transform into the Mn^{3+} areas owing to the intercalation of zinc ions. Figure S13 delivers the XPS spectra of Ag 3d, O 1s, and Zn 2p at fully discharged and charged states, verifying the regular change of valence states of the component elements. As exhibited in Figure 4c, the crystalline phase of AgCl can be first detected when initially charged to 1.5 V, hold the highest diffraction intensity when initially charged to 1.8 V, and stably exist during the subsequent discharge process. In addition, the weak diffraction peaks at 28.9° and 37.5° can be assigned to the (310) and (211) characteristic peaks of the $Ag_{2-x}Mn_8O_{16}$ cathode, respectively, which regularly shift along with the insertion and extraction of zinc ions. Furthermore, the XRD patterns (Figure S14), HRTEM image (Figure S15a), and elemental mapping images (Figure S15b) of $Ag_2Mn_8O_{16}$ cathode after 100 cycles have been supplemented. In detail, four diffraction peaks at 25.8°, 28.9°, 37.5°, and 46.1° can be assigned to the (220), (310), (211), and (321) peaks of $Ag_{2-x}Mn_8O_{16}$, respectively, while the (111) and (200) characteristic peaks of AgCl appear at 27.8° and 32.2°. The (310) characteristic peaks of $Ag_{2-x}Mn_8O_{16}$ and the (200) characteristic peaks of AgCl can be further detected in the HRTEM image (Figure S15a), and the elemental mapping images (Figure S15b) of Ag,

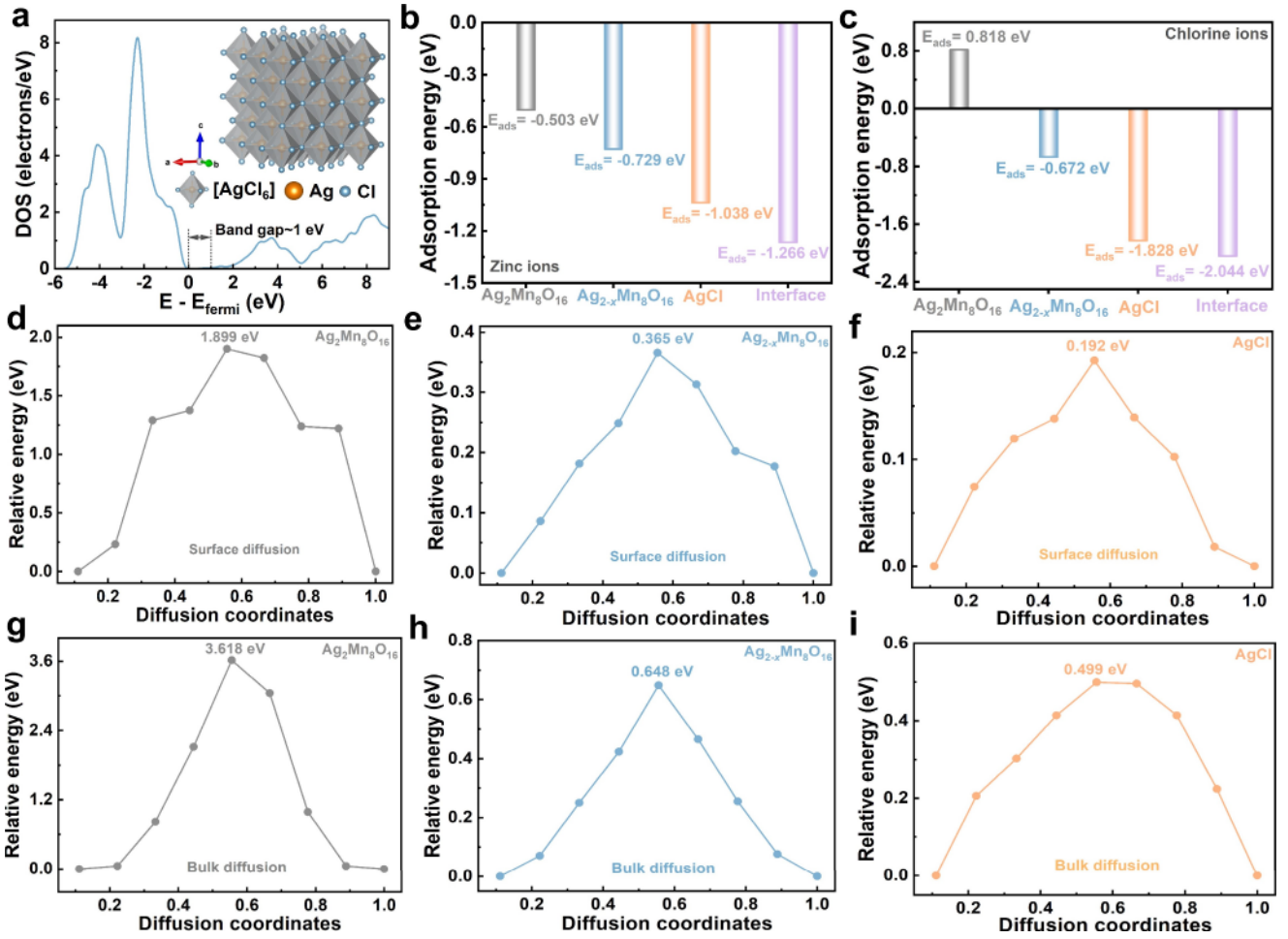

Figure 6. (a) Density of states (DOS) of AgCl material; adsorption energy for (b) zinc ions and (c) chlorine ions on the surface of $Ag_2Mn_8O_{16}$, $Ag_{2-x}Mn_8O_{16}$, and AgCl and the phase interface between AgCl and $Ag_{2-x}Mn_8O_{16}$; diffusion energy barriers of zinc ions on the surface of the crystalline structure of (d) $Ag_2Mn_8O_{16}$, (e) $Ag_{2-x}Mn_8O_{16}$, and (f) AgCl; diffusion energy barriers of zinc ions inside the crystalline structure of (g) $Ag_2Mn_8O_{16}$, (h) $Ag_{2-x}Mn_8O_{16}$, and (i) AgCl.

Mn, O, Cl, and Zn also can intuitively certify the stable existence of the AgCl layer, which can effectively inhibit the manganese dissolution, stabilize the crystal structure, and maintain the cyclic stability of the $Ag_2Mn_8O_{16}$ cathode.

The phase transformation of the $Ag_2Mn_8O_{16}$ cathode can be further characterized by the HRTEM images at the fully charged and discharged state. As presented in Figure 4d, the (310) characteristic peaks of $Ag_{2-x}Mn_8O_{16}$ and the (111) characteristic peaks of AgCl can be detected in the inside and outside region, respectively. Similarly, the (310) and (101) characteristic peaks of $Ag_{2-x}Mn_8O_{16}$ and the (200) characteristic peaks of AgCl can be found in the fully discharged state (Figure 4f), manifesting the stable existence of AgCl after initial anodic oxidation. Notably, the interplanar spacing corresponding to the characteristic peaks of $Ag_{2-x}Mn_8O_{16}$, i.e., 0.27 and 0.304 nm for (101) and (310) crystal planes, respectively, are smaller than that of raw $Ag_2Mn_8O_{16}$ material (0.308 nm for (310) crystal plane), demonstrating that the partial deintercalation of silver ions weakens the electrostatic repulsion in the crystal structure and reduces the lattice spacing.[48] Additionally, the elemental mapping images of Ag, Mn, O, Cl, and Zn at fully charged (Figure 4e) and discharged (Figure 4g) states also can intuitively testify to the formation and crystal phase stabilization of AgCl during the cycling process. According to the characterization analysis, the protection mechanism of the AgCl interface layer on the $Ag_2Mn_8O_{16}$ cathode during the cycling process can be schematically illustrated as in Figure 5. The partial deintercalation of silver ions from $Ag_2Mn_8O_{16}$ during the initial charge process and the following precipitation reaction between silver ions and chlorine ions in the electrolyte jointly facilitate the spontaneous formation of AgCl interface layer, which is beneficial to the inhibition of manganese dissolution, fast migration of zinc ions, low activation energy barrier of interface reaction, and durable cycling stability of the $Ag_2Mn_8O_{16}$ cathode.

To deeply understand the theoretical properties and multiple effects of the AgCl SEI layer, detailed DFT calculations have been performed. Figure 6a and Figure S16 respectively present the density of states (DOS), energy band structure, and electron conductivity of AgCl material, and AgCl possesses a simulated band gap of 1.0 eV, determining its inferior electrical conductivity and electronic insulation property. The insert image in Figure 6a is the crystal structure of AgCl material, which is halite structured and crystallizes in the cubic $Fm\bar{3}m$ space group, and Ag atoms are bonded to six equivalent Cl atoms to form a mixture of corner and edge-sharing $[AgCl_6]$ octahedra with an ionic bond length of 2.77 Å for Ag−Cl. As shown in Figure 6b and Figure S17, the adsorption energy of zinc ions on the surface of $Ag_2Mn_8O_{16}$,

$Ag_{2-x}Mn_8O_{16}$, and AgCl and the phase interface between AgCl and $Ag_{2-x}Mn_8O_{16}$ have been explored. As a result, the adsorption energies of $Ag_{2-x}Mn_8O_{16}$, AgCl, and their phase interface for zinc ions are −0.729, −1.038, and −1.266 eV, respectively, which are thermodynamically stronger than that of the raw $Ag_2Mn_8O_{16}$ material (−0.503 eV), indicating the enhanced zinc adsorption behavior after the partial extraction of silver ions from $Ag_2Mn_8O_{16}$ and the *in situ* formation of a AgCl SEI layer. Additionally, the corresponding adsorption energies of chlorine ions on the above positions also have been investigated in Figure 6c and Figure S18. The calculated adsorption energy of $Ag_2Mn_8O_{16}$, $Ag_{2-x}Mn_8O_{16}$, AgCl, and their phase interface for chlorine ions are 0.818, −0.672, −1.828, and −2.044 eV, respectively, manifesting that the partial deintercalation of silver ions and the formation of AgCl layer can promote the chlorine adsorption behavior, which is essential for the redox reaction of chlorine ions.[49] This interesting result well explains the differences in characteristic peaks (1.083/0.864 V) of CV curves measured in chlorine-containing and chlorine-free electrolytes. Moreover, the diffusion energy barriers of zinc ions both on the surface and inside the crystalline structure of $Ag_2Mn_8O_{16}$, $Ag_{2-x}Mn_8O_{16}$, and AgCl have been calculated. As exhibited in Figures 6d−f and Figure S19, the surface zinc diffusion energy barriers of $Ag_{2-x}Mn_8O_{16}$ and AgCl are 0.365 and 0.192 eV, respectively, which are much lower than that of $Ag_2Mn_8O_{16}$ (1.899 eV), demonstrating that the partial deintercalation of silver ions can facilitate the zinc diffusion kinetics of $Ag_2Mn_8O_{16}$, and the AgCl layer has intrinsic ionic conductor property as well as fast zinc migration kinetics. Figures 6g−i and S20−S22 respectively present the bulk zinc diffusion energy barriers and diffusion paths of $Ag_2Mn_8O_{16}$ (3.618 eV), $Ag_{2-x}Mn_8O_{16}$ (0.648 eV), and AgCl (0.499 eV), which are higher than the corresponding surface diffusion energy barriers, implying that the bulk diffusion of zinc ions is more difficult than the surface diffusion. Notably, $Ag_{2-x}Mn_8O_{16}$ exhibits a lower bulk diffusion energy barrier than $Ag_2Mn_8O_{16}$, verifying that the partial deintercalation of silver ions favors the zinc migration behavior. In addition, AgCl also delivers the lowest bulk diffusion energy barrier, further confirming its fast zinc diffusion kinetics both on the surface and inside the crystal structure. The above theoretical calculations verify that AgCl is an ideal SEI layer for $Ag_2Mn_8O_{16}$ cathode in an aqueous electrolyte, which can act as robust armor to prevent the erosion of active solvent molecules, inhibit the manganese dissolution, and guarantee the cycling stability of aqueous batteries.[50−52]

In summary, a promising manganese-based material of $Ag_2Mn_8O_{16}$ is employed as the cathode candidate for AZIBs. The influences of charge/discharge modes and electrolyte compositions on the zinc storage performances of the $Ag_2Mn_8O_{16}$ cathode have been deeply investigated. Combining the charge before discharge mode with a chlorine-containing electrolyte, the partial deintercalation of silver ions and the formation of a AgCl SEI layer can spontaneously occur on the surface of the $Ag_{2-x}Mn_8O_{16}$ cathode during the initial charge process, which can suppress the manganese dissolution, reduce the interface impedance, and facilitate the adsorption behavior of chlorine ions as well as migration behavior of zinc ions. Moreover, the partial deintercalation of silver ions during the initial charge process also can effectively promote the valence state and reactivity of Mn element in $Ag_{2-x}Mn_8O_{16}$ cathode and improve the zinc storage capacity. Owing to these merits, $Zn//Ag_2Mn_8O_{16}$ batteries can display high reversible capacity of 369.2 mAh g^{-1} at 100 mA g^{-1}, 269.6 mAh g^{-1} after 200 cycles at 500 mA g^{-1}, and 167.8 mAh g^{-1} after 409 cycles at 1000 mA g^{-1} in 2 M $ZnSO_4$ + 0.1 M $MnSO_4$ + 0.1 M $ZnCl_2$ electrolyte, delivering superior zinc storage performance and durable structure stability. This work will open the door for *in situ* interface engineering of cathode materials in aqueous electrolytes and pave the way for practical application of aqueous rechargeable batteries.

AUTHOR INFORMATION

Corresponding Authors

Lutong Shan − *Department of Chemistry, University of Manchester, Manchester M139PL, U.K.*; Email: lutong.shan@postgrad.manchester.ac.uk

Huangxu Li − *Department of Applied Physics and Research Institute for Smart Energy, The Hong Kong Polytechnic University, Hung Hom, Kowloon, Hong Kong SAR, China*; Email: huangxu.li@polyu.edu.hk

Xinlong Tian − *School of Marine Science and Engineering, State Key Laboratory of Marine Resource Utilization in South China Sea, Hainan University, Haikou 570228, China*; orcid.org/0000-0001-8388-5198; Email: tianxl@hainanu.edu.cn

Authors

Xiaodong Shi − *School of Marine Science and Engineering, State Key Laboratory of Marine Resource Utilization in South China Sea, Hainan University, Haikou 570228, China*

Chuancong Zhou − *School of Marine Science and Engineering, State Key Laboratory of Marine Resource Utilization in South China Sea, Hainan University, Haikou 570228, China*

Fuhua Yang − *Helmholtz Institute Ulm, D-89081 Ulm, Germany*

Boya Tang − *Department of Chemistry, University of Manchester, Manchester M139PL, U.K.*

Jie Zhang − *School of Marine Science and Engineering, State Key Laboratory of Marine Resource Utilization in South China Sea, Hainan University, Haikou 570228, China*

Qing Nan − *School of Marine Science and Engineering, State Key Laboratory of Marine Resource Utilization in South China Sea, Hainan University, Haikou 570228, China*

Yu Xie − *School of Marine Science and Engineering, State Key Laboratory of Marine Resource Utilization in South China Sea, Hainan University, Haikou 570228, China*

Jing Li − *School of Marine Science and Engineering, State Key Laboratory of Marine Resource Utilization in South China Sea, Hainan University, Haikou 570228, China*

Author Contributions

[#]X.S. and C.Z. contributed equally.

Notes

The authors declare no competing financial interest.

■ ACKNOWLEDGMENTS

The authors acknowledge the financial support of the National Natural Science Foundation of China (52274297 and 52164028), the specific research fund of the Innovation Platform for Academicians of Hainan Province (YSPTZX202315), the Foundation of State Key Laboratory of Marine Resource Utilization in South China Sea (Hainan University, Grant No. MRUKF2021029), and the Start-up Research Foundation of Hainan University (KYQD(ZR)-23069 and 20008). Especially, Lutong Shan and Boya Tang thank the China Scholarship Council for funding support.

■ REFERENCES

(1) Gao, Y.; Zhou, J.; Qin, L.; Xu, Z.; Liu, Z.; Wang, L.; Cao, X.; Fang, G.; Liang, S. Crystal plane induced in-situ electrochemical activation of manganese-based cathode enable long-term aqueous zinc-ion batteries. *Green Energy Environ.* **2023**, *8* (5), 1429−1436.

(2) Xue, T.; Fan, H. J. From aqueous Zn-ion battery to Zn-MnO_2 flow battery: A brief story. *J. Energy Chem.* **2021**, *54*, 194−201.

(3) Feng, Z.; Zhang, Y.; Gao, Z.; Hu, D.; Jiang, H.; Hu, T.; Meng, C.; Zhang, Y. Construction interlayer structure of hydrated vanadium oxides with tunable P-band center of oxygen towards enhanced aqueous Zn-ion batteries. *Adv. Powder Mater.* **2024**, *3* (2), 100167.

(4) Yang, F.; Yuwono, J. A.; Hao, J.; Long, J.; Yuan, L.; Wang, Y.; Liu, S.; Fan, Y.; Zhao, S.; Davey, K.; et al. Understanding H_2 evolution electrochemistry to minimize solvated water impact on zinc-anode performance. *Adv. Mater.* **2022**, *34* (45), 2206754.

(5) Zhang, A.; Zhao, R.; Wang, Y.; Yang, J.; Wu, C.; Bai, Y. Regulating the electronic structure of manganese-based materials to optimize the performance of zinc-ion batteries. *Energy Environ. Sci.* **2023**, *16* (8), 3240−3301.

(6) Yao, H.; Yu, H.; Zheng, Y.; Li, N. W.; Li, S.; Luan, D.; Lou, X. W.; Yu, L. Pre-intercalation of ammonium ions in layered δ-MnO_2 nanosheets for high-performance aqueous zinc-ion batteries. *Angew. Chem., Int. Ed.* **2023**, *62*, e202315257.

(7) Li, G.; Sun, L.; Zhang, S.; Zhang, C.; Jin, H.; Davey, K.; Liang, G.; Liu, S.; Mao, J.; Guo, Z. Developing cathode materials for aqueous zinc ion batteries: challenges and practical prospects. *Adv. Funct. Mater.* **2024**, *34*, 2301291.

(8) Zhang, N.; Wang, J. C.; Guo, Y. F.; Wang, P. F.; Zhu, Y. R.; Yi, T. F. Insights on rational design and energy storage mechanism of Mn-based cathode materials towards high performance aqueous zinc-ion batteries. *Coordin. Chem. Rev.* **2023**, *479*, 215009.

(9) Zhang, Y. A.; Liu, Y. P.; Liu, Z. H.; Wu, X. G.; Wen, Y. X.; Chen, H. D.; Ni, X.; Liu, G. H.; Huang, J. J.; Peng, S. L. MnO_2 cathode materials with the improved stability via nitrogen doping for aqueous zinc-ion batteries. *J. Energy Chem.* **2022**, *64*, 23−32.

(10) Chen, Q.; Lou, X.; Yuan, Y.; You, K.; Li, C.; Jiang, C.; Zeng, Y.; Zhou, S.; Zhang, J.; Hou, G.; et al. Surface adsorption and proton chemistry of ultra-stabilized aqueous zinc-manganese dioxide batteries. *Adv. Mater.* **2023**, *35*, 2306294.

(11) Zhang, T.; Tang, Y.; Fang, G.; Zhang, C.; Zhang, H.; Guo, X.; Cao, X.; Zhou, J.; Pan, A.; Liang, S. Electrochemical activation of manganese-based cathode in aqueous zinc-ion electrolyte. *Adv. Funct. Mater.* **2020**, *30* (30), No. 2002711.

(12) Kang, S.; Cho, S.; Kang, Y. M. Getting to the bottom of transition metal dissolution. *Nat. Nanotechnol.* **2023**, *18*, 700−710.

(13) Zhu, X.; Meng, F.; Zhang, Q.; Xue, L.; Zhu, H.; Lan, S.; Liu, Q.; Zhao, J.; Zhuang, Y.; Guo, Q.; et al. $LiMnO_2$ cathode stabilized by interfacial orbital ordering for sustainable lithium-ion batteries. *Nat. Sustain.* **2021**, *4* (5), 392−401.

(14) Liu, S.; Wang, B.; Zhang, X.; Zhao, S.; Zhang, Z.; Yu, H. Reviving the lithium-manganese-based layered oxide cathodes for lithium-ion batteries. *Matter* **2021**, *4* (5), 1511−1527.

(15) Zhou, W.; Fan, H. J.; Zhao, D.; Chao, D. Cathodic electrolyte engineering toward durable Zn-Mn aqueous batteries. *Natl. Sci. Rev.* **2023**, *10* (12), No. nwad265.

(16) Fang, G.; Zhu, C.; Chen, M.; Zhou, J.; Tang, B.; Cao, X.; Zheng, X.; Pan, A.; Liang, S. Suppressing manganese dissolution in potassium manganate with rich oxygen defects engaged high-energy-density and durable aqueous zinc-ion battery. *Adv. Funct. Mater.* **2019**, *29* (15), No. 1808375.

(17) Ren, Q.; Yuan, Y.; Wang, S. Interfacial strategies for suppression of Mn dissolution in rechargeable battery cathode materials. *ACS Appl. Mater. Interfaces* **2022**, *14* (20), 23022−23032.

(18) Wu, B.; Zhang, G.; Yan, M.; Xiong, T.; He, P.; He, L.; Xu, X.; Mai, L. Graphene scroll-coated α-MnO_2 nanowires as high-performance cathode materials for aqueous Zn-ion battery. *Small* **2018**, *14* (13), No. 1703850.

(19) Liu, Y.; Qin, Z.; Yang, X.; Sun, X. A long-life manganese oxide cathode material for aqueous zinc batteries with a negatively charged porous host to promote the back-deposition of dissolved Mn^{2+}. *Adv. Funct. Mater.* **2022**, *32* (10), No. 2106994.

(20) Yan, L. J.; Liu, B. B.; Hao, J. Y.; Han, Y. Y.; Zhu, C.; Liu, F. L.; Zou, X. F.; Zhou, Y.; Xiang, B. In-situ cation-inserted MnO_2 with selective accelerated intercalation of individual H^+ or Zn^{2+} ions in aqueous zinc ion batteries. *J. Energy Chem.* **2023**, *82*, 88−102.

(21) Li, G.; Huang, Z.; Chen, J.; Yao, F.; Liu, J.; Li, O. L.; Sun, S.; Shi, Z. Rechargeable Zn-ion batteries with high power and energy densities: A two-electron reaction pathway in birnessite MnO_2 cathode materials. *J. Mater. Chem. A* **2020**, *8* (4), 1975−1985.

(22) Ding, S.; Zhang, M.; Qin, R.; Fang, J.; Ren, H.; Yi, H.; Liu, L.; Zhao, W.; Li, Y.; Yao, L.; et al. Oxygen-deficient β-MnO_2@ graphene oxide cathode for high-rate and long-life aqueous zinc ion batteries. *Nano-Micro Lett.* **2021**, *13* (1), 173.

(23) Luo, H.; Wang, L.; Ren, P.; Jian, J.; Liu, X.; Niu, C.; Chao, D. Atomic engineering promoted electrooxidation kinetics of manganese-based cathode for stable aqueous zinc-ion batteries. *Nano Res.* **2022**, *15* (9), 8603−8612.

(24) Fu, Y.; Wei, Q.; Zhang, G.; Wang, X.; Zhang, J.; Hu, Y.; Wang, D.; Zuin, L.; Zhou, T.; Wu, Y. High-performance reversible aqueous Zn-ion battery based on porous MnO_x nanorods coated by MOF-derived N-doped carbon. *Adv. Energy Mater.* **2018**, *8* (26), No. 1801445.

(25) Xiao, X.; Wang, T.; Zhao, Y.; Gao, W.; Wang, S. A design of MnO-CNT@C_3N_4 cathodes for high-performance aqueous zinc-ion batteries. *J. Colloid Interface Sci.* **2023**, *642*, 340−350.

(26) Deng, S.; Tie, Z.; Yue, F.; Cao, H.; Yao, M.; Niu, Z. Rational design of $ZnMn_2O_4$ quantum dots in a carbon framework for durable aqueous zinc-ion batteries. *Angew. Chem., Int. Ed.* **2022**, *134* (12), No. e202115877.

(27) Ye, F.; Liu, Q.; Lu, C.; Meng, F.; Lin, T.; Dong, H.; Gu, L.; Wu, Y.; Tang, Z.; Hu, L. Inorganic manganese oxide/quinone coupling for high-capacity aqueous Zn-ion battery. *Energy Storage Mater.* **2022**, *52*, 675−684.

(28) Zhao, Y.; Zhou, R.; Song, Z.; Zhang, X.; Zhang, T.; Zhou, A.; Wu, F.; Chen, R.; Li, L. Interfacial designing of MnO_2 half-wrapped by aromatic polymers for high-performance aqueous zinc-ion batteries. *Angew. Chem., Int. Ed.* **2022**, *61* (49), No. e202212231.

(29) Huang, J.; Tang, X.; Liu, K.; Fang, G.; He, Z.; Li, Z. Interfacial chemical binding and improved kinetics assisting stable aqueous Zn-MnO_2 batteries. *Mater. Today Energy* **2020**, *17*, No. 100475.

(30) Li, Z.; Zheng, Y.; Jiao, Q.; Zhao, Y.; Li, H.; Feng, C. Tailoring porous three-dimensional $(Co, Mn)_2O_4$/PPy architecture towards high-performance cathode for aqueous zinc-ion batteries. *Chem. Eng. J.* **2023**, *465*, No. 142897.

(31) Shi, M.; Wang, B.; Chen, C.; Lang, J.; Yan, C.; Yan, X. 3D high-density MXene@MnO_2 microflowers for advanced aqueous zinc-ion batteries. *J. Mater. Chem. A* **2020**, *8* (46), 24635−24644.

(32) Wang, H.; Guo, R.; Ma, Y.; Zhou, F. Cross-doped Mn/Mo oxides with core-shell structures designed by a self-template strategy for durable aqueous zinc-ion batteries. *Adv. Funct. Mater.* **2023**, *33*, 2301351.

(33) Yang, T.; Niu, Y.; Liu, Q.; Xu, M. Cathode host engineering for non-lithium (Na, K and Mg) sulfur/selenium batteries: A state-of-the-art review. *Nano Mater. Sci.* **2023**, *5* (2), 119−140.
(34) Wan, Y.; Liu, Y.; Chao, D.; Li, W.; Zhao, D. Recent advances in hard carbon anodes with high initial Coulombic efficiency for sodium-ion batteries. *Nano Mater. Sci.* **2023**, *5* (2), 189−201.
(35) Chen, F.; Xu, Z. L. Design and manufacture of high-performance microbatteries: lithium and beyond. *Microstructures* **2022**, *2* (10), 2022012.
(36) Guo, S.; Liang, S.; Zhang, B.; Fang, G.; Ma, D.; Zhou, J. Cathode interfacial layer formation via in situ electrochemically charging in aqueous zinc-ion battery. *ACS Nano* **2019**, *13* (11), 13456−13464.
(37) Dai, L.; Nie, X.; Sun, Q.; Li, D.; Yao, Y.; Guo, H.; Li, J.; Xiao, S.; Liao, J.; Lu, J.; et al. One-step synthesis of hollow urchin-like $Ag_2Mn_8O_{16}$ for long-life Li-O_2 battery. *J. Alloy. Compd.* **2022**, *892*, No. 162137.
(38) Li, J.; Luo, N.; Kang, L.; Zhao, F.; Jiao, Y.; Macdonald, T. J.; Wang, M.; Parkin, I. P.; Shearing, P. R.; Brett, D. J.; et al. Hydrogen-bond reinforced superstructural manganese oxide As the cathode for ultra-stable aqueous zinc ion batteries. *Adv. Energy Mater.* **2022**, *12* (44), No. 2201840.
(39) Ding, J.; Du, H.; Cai, G.; Huang, S.; Peng, C.; Wang, L.; Luo, J.; Wang, X.; Xue, M.; Zhang, X.; et al. Layer symmetry and interlayer engineering of birnessites towards high-performance rechargeable aqueous Zn-MnO_2 batteries. *Nano Energy* **2023**, *112*, No. 108485.
(40) Yu, J.; Li, B. Q.; Zhao, C. X.; Zhang, Q. Seawater electrolyte-based metal-air batteries: from strategies to applications. *Energy Environ. Sci.* **2020**, *13* (10), 3253−3268.
(41) Chen, J.; Shi, X.; Feng, S.; Li, J.; Gao, X.; Wu, X.; Li, K.; Qi, A.; You, C.; Tian, X. Design of highly active and durable oxygen evolution catalyst with intrinsic chlorine inhibition property for seawater electrolysis. *Nano Mater. Sci.* **2023**, DOI: 10.1016/j.nanoms.2023.10.003.
(42) Xie, X.; Fu, H.; Fang, Y.; Lu, B.; Zhou, J.; Liang, S. Manipulating ion concentration to boost two-electron Mn^{4+}/Mn^{2+} redox kinetics through a colloid electrolyte for high-capacity zinc batteries. *Adv. Energy Mater.* **2022**, *12* (5), No. 2102393.
(43) Pan, Y.; Liu, Z.; Liu, S.; Qin, L.; Yang, Y.; Zhou, M.; Sun, Y.; Cao, X.; Liang, S.; Fang, G. Quasi-decoupled solid-liquid hybrid electrolyte for highly reversible interfacial reaction in aqueous zinc-manganese battery. *Adv. Energy Mater.* **2023**, *13* (11), No. 2203766.
(44) Wang, S.; Ru, Y.; Sun, Y.; Pang, H. Fan-like MnV_2O_6 superstructure for rechargeable aqueous zinc ion batteries. *Chin. Chem. Lett.* **2023**, *34*, 108143.
(45) Yang, H.; Zhang, T.; Chen, D.; Tan, Y.; Zhou, W.; Li, L.; Li, W.; Li, G.; Han, W.; Fan, H. J.; et al. Protocol in evaluating capacity of Zn-Mn aqueous batteries: A clue of pH. *Adv. Mater.* **2023**, *35*, 2300053.
(46) Yuan, Y.; Sharpe, R.; He, K.; Li, C.; Saray, M. T.; Liu, T.; Yao, W.; Cheng, M.; Jin, H.; Wang, S.; et al. Understanding intercalation chemistry for sustainable aqueous zinc-manganese dioxide batteries. *Nat. Sustain.* **2022**, *5* (10), 890−898.
(47) Hu, Y.; Liu, Z.; Li, L.; Guo, S.; Xie, X.; Luo, Z.; Fang, G.; Liang, S. Reconstructing interfacial manganese deposition for durable aqueous zinc-manganese batteries. *Natl. Sci. Rev.* **2023**, *10* (10), No. nwad220.
(48) Zhang, A.; Wang, X.; Zhao, R.; Wang, Y.; Yue, J.; Yang, J.; Wu, C.; Bai, Y. Hybrid superlattice-triggered electron-entropy stimulation and selective proton Grotthuss-intercalation in polymer-intercalated δ-MnO_2 for high-performance Zn-MnO_2 battery. *Angew. Chem., Int. Ed.* **2023**, *62*, e202313163.
(49) Zhao, Y.; Yang, C.; Yu, Y. A review on covalent organic frameworks for rechargeable zinc-ion batteries. *Chin. Chem. Lett.* **2023**, No. 108865.
(50) Zuo, Y.; Meng, T.; Tian, H.; Ling, L.; Zhang, H.; Zhang, H.; Sun, X.; Cai, S. Enhanced H^+ storage of a MnO_2 cathode via a MnO_2 nanolayer interphase transformed from manganese phosphate. *ACS Nano* **2023**, *17* (6), 5600−5608.
(51) Yang, H.; Zhou, W.; Chen, D.; Liu, J.; Yuan, Z.; Lu, M.; Shen, L.; Shulga, V.; Han, W.; Chao, D. The origin of capacity fluctuation and rescue of dead Mn-based Zn−ion batteries: a Mn-based competitive capacity evolution protocol. *Energ Environ. Sci.* **2022**, *15* (3), 1106−1118.
(52) Hu, Y.; Fu, C.; Chai, S.; He, Q.; Wang, Y.; Feng, M.; Zhang, Y.; Pan, A. Construction of zinc metal-Tin sulfide polarized interface for stable Zn metal batteries. *Adv. Powder Mater.* **2023**, *2* (2), No. 100093.